Disproportionation, Dopant Incorporation, and Defect Clustering in Perovskite-Structured NdCoO 3

ARTICLE *in* THE JOURNAL OF PHYSICAL CHEMISTRY B · APRIL 2006

Impact Factor: 3.3 · DOI: 10.1021/jp0571325 · Source: PubMed

4 AUTHORS, INCLUDING:

Lorenzo Malavasi
University of Pavia
160 PUBLICATIONS **1,638** CITATIONS
SEE PROFILE

Craig A. J. Fisher
Japan Fine Ceramics Center
79 PUBLICATIONS **2,114** CITATIONS
SEE PROFILE

M. Saiful Islam
University of Bath
175 PUBLICATIONS **7,435** CITATIONS
SEE PROFILE

Disproportionation, Dopant Incorporation, and Defect Clustering in Perovskite-Structured $NdCoO_3$

Cristina Tealdi,[†] Lorenzo Malavasi,[†] Craig A. J. Fisher,[‡] and M. Saiful Islam*[,§]

Dipartimento di Chimica Fisica "M. Rolla", Università di Pavia, Viale Taramelli 16, 27100 Pavia, Italy, Chemistry Division, SBMS, University of Surrey, Guildford, GU2 7XH, United Kingdom, and Department of Chemistry, University of Bath, Bath, BA2 7AY, United Kingdom

Received: December 7, 2005; In Final Form: January 26, 2006

Atomistic simulation techniques are used to examine the defect chemistry of perovskite-structured $NdCoO_3$, a material whose electrochemical properties make it attractive for use in heterogeneous oxidation catalysis, as well as in gas sensors and mixed ionic/electronic conductors. In practice, dopants are added to $NdCoO_3$ to obtain the desired properties, such as high electrical conductivity and rapid gas adsorption/desorption; thus, a wide range of dopants substituted on both Nd and Co sites are examined. Charge compensation for aliovalent dopants is predicted to occur via formation of oxide ion vacancies; these are understood to be key sites with respect to catalytic and sensor activity. Low activation energies calculated for oxide ion migration are consistent with high oxygen mobilities measured experimentally. Sr and Ca, which occupy Nd sites in the lattice, are found to be the most soluble of the alkaline earth metals, in agreement with experiment. These two dopant ions also have the weakest binding energies for dopant-vacancy cluster formation. Mechanisms of electronic defect formation, critical to the overall transport properties of the material, are also considered. The results suggest that disproportionation of the Co ion to form small polaron species is the most favorable intrinsic defect process. In doped compounds, formation of electronic holes via uptake of oxygen at vacant sites is found to be a low energy process.

1. Introduction

Perovskite-type oxides, ABO_3, with rare earth ions (particularly La) on the A site and transition-metal ions on the B site, have been the subject of intense research over the past decade partly because their electrical, magnetic, optical, and chemical properties can be improved dramatically by doping. The range of possible applications for these mixed-conducting oxides is wide, extending from components in solid oxide fuel cells (SOFCs),[1] oxygen separation membranes, and electrochemical reactors[2,3] to sensor devices and catalysts that oxidize CO and CH_4 or reduce NO.[4−6] In addition, in recent years there has been increasing interest in cobalt-containing perovskites because of their unusual thermoelectric behavior[7−9] and ability to exhibit colossal magnetoresistance (CMR).[10−13] Compared with the $LaCoO_3$ system, $NdCoO_3$ has been the subject of relatively few studies.[14−18] However, the similarity between the neodymium cobaltite and its lanthanum analog, particularly in terms of crystal structures and electrical and magnetic behavior, means that $LaCoO_3$ provides a useful starting point for the study of $NdCoO_3$.

Defect chemistry is one of the key aspects to understanding the various properties of $NdCoO_3$. It is well-known that manganites and cobaltites have different degrees of oxygen nonstoichiometry under the same conditions[19,20] (i.e., different values of δ in $ABO_{3-\delta}$, where B = Mn or Co and A = rare earth), which directly relates to the number of oxygen vacancies in the structure. Manganites tend to be super-stoichiometric, whereas cobaltites are usually sub-stoichiometric, because of the different redox stabilities of the B cation. The number of intrinsic oxygen vacancies at room temperature has a direct effect on the transport and catalytic properties of these oxides.[20]

In general, cobaltites are more catalytically active than manganites because of their higher concentration of oxygen vacancies.[21] A model has been proposed in which the large number of oxygen vacancies in the cobaltites form ordered clusters, microdomains or ordered phases.[19] Under reducing conditions, and as temperature increases, more oxygen vacancies are created by removal of oxide ions at the surface to form gaseous molecular oxygen. Similar to $LaCoO_3$, the electrical conductivity of $NdCoO_3$ is known to exhibit a complex temperature dependence. In the case of $LaCoO_3$, this is understood to be a result of disproportionation of the Co ion,[22] and the same phenomenon is known to take place in $NdCoO_3$.[23] The presence of different electronic species resulting from this disproportionation reaction can also be expected to have an important influence on the redox properties of these oxides.

The overall oxygen transport in $NdCoO_3$-based compounds will be controlled by the interaction between two processes: oxygen diffusion in the bulk phase and exchange of oxygen with the atmosphere at the surface. For a mixed conductor, incorporation of oxygen gas at the surface occurs when an oxygen molecule dissociates into two oxide ions that enter vacant sites in the crystal lattice with the formation of electronic species. This reaction will occur in a number of steps, including adsorption, dissociation, charge transfer, and migration of the oxygen into the bulk phase.[24] For this to occur rapidly, there must be sufficient oxygen mobility in the lattice to facilitate exchange between adsorbed oxygen, surface lattice oxygen, and the bulk lattice oxygen. In other words, the mobility of the lattice oxygen plays an important role in the overall surface-exchange process.

* To whom correspondence should be addressed. Phone: +44-1225-384938; Fax: +44-1225-386231; E-mail: m.s.islam@bath.ac.uk.
[†] Università di Pavia.
[‡] University of Surrey.
[§] University of Bath.

10.1021/jp0571325 CCC: $33.50
Published on Web 02/23/2006

Our recent work[25] has highlighted the possibility of using $NdCoO_3$ as a CO-gas sensing material. However, without a proper understanding of the defect structure of this phase, it is difficult to determine the mechanisms involved in its sensing behavior, making optimization of its properties difficult. The aim of this work is to elucidate, by means of advanced simulation techniques, the defect chemistry and redox processes of perovskite-structured $NdCoO_3$ at the atomic level. Our simulation methods, which have been applied successfully to a range of complex ternary oxides,[26−29] are outlined in the next section. After comparing the energetics of various possible intrinsic defects, we examine oxide ion migration in the bulk structure. To determine the likely electronic species in the material (because these will govern the amount and nature of any electronic conductivity), the energetics of various redox processes are also considered. In the last section, we focus our attention on the effect of doping of the system because of its importance for optimizing the properties of $NdCoO_3$. In addition to comparing relative solubilities of different dopant cations, our simulation techniques enable us to predict whether clustering of defects, a phenomenon frequently observed in other doped systems, is likely to be significant for the range of dopants considered.

2. Simulation Methods

The simulation techniques used in this work are based upon lattice energy minimization procedures, embodied in the code GULP.[30] Only a brief summary of the key aspects of these techniques will be presented, as comprehensive reviews are given elsewhere.[31]

The simulations are based upon the specification of a potential model that describes the energy of the system as a function of the atomic coordinates and allows the modeling of perfect and defective lattices. The interactions between ions are partitioned into long-range Coulombic forces and short-range forces that account for electron cloud overlap (Pauli repulsion) and van der Waals interactions. The short-range interactions, ϕ, were modeled with a Buckingham potential of the form:

$$\phi_{ij} = A_{ij} \exp(-r/\rho_{ij}) - C_{ij}/r^6 \quad (1)$$

where A_{ij}, ρ_{ij}, and C_{ij} are the potential parameters between ions of type i and j, and r is the distance between each ion pair.

Ion polarizability was treated using the "shell" model developed by Dick and Overhauser.[32] In this model, each ion is represented as a massless shell of charge Y connected by an elastic spring of constant K to a massive core. The sum of the charges of the shell and core is equal to the formal charge of the ion. The coupling between the short-range repulsive forces and electronic polarization that this introduces has been found to simulate effectively both dielectric and elastic properties of polar solids.

Lattice relaxation around a charged defect typically causes extensive perturbation of the surrounding lattice. Defect modeling of such effects was performed using the two-region Mott−Littleton method.[31] Using this approach, the crystal lattice was partitioned into a spherical inner region (region I) of more than 500 ions with the defect at its center and an outer region extending to infinity (region II). Whereas in region I the interactions between ions were calculated explicitly, the response of region II to the defect was treated by more approximate quasi-continuum methods, because at these distances, the forces are relatively weak.

Before carrying out defect and migration calculations, the cubic perovskite structure of $NdCoO_3$[33] was equilibrated under constant pressure to find the local energy minimum. The interatomic potentials used are reported in Table 1, in which the $Co^{3+}\cdots O^{2-}$ and the $O^{2-}\cdots O^{2-}$ parameters are from previous studies on cobalt-containing perovskites.[34] The $Nd^{3+}\cdots O^{2-}$ parameters were also taken from earlier work,[35] with the ρ term modified slightly to better reproduce the experimentally observed structure. The same set of potentials also successfully reproduced the orthorhombic structure of $NdCoO_3$,[36] and a comparison between the experimental and the calculated structures for both cubic and orthorhombic phases is reported in Table 2. The excellent agreement between our simulated structures and experimental data suggests that the set of potentials used in this study is sufficiently reliable for the subsequent defect calculations.

TABLE 1: Interatomic Potential and Shell-Model Parameters for $NdCoO_3$

interaction	A (eV)	ρ (Å)	C (eV Å^6)	Y (e)	K (eV Å^{-2})
$Nd^{3+}\cdots O^{2-}$	1379.90	0.36072	22.59	0.00	99999.0
$Co^{3+}\cdots O^{2-}$	1329.82	0.30870	0.00	2.04	196.3
$O^{2-}\cdots O^{2-}$	22764.30	0.14900	43.00	−2.24	42.0

TABLE 2: Experimental and Calculated Structural Parameters of Cubic and Orthorhombic $NdCoO_3$

Cubic Structure			
parameters	exp/Å	calcd/Å	Δ (exp − calcd)/Å
a	3.770	3.770	0.000
Nd−O	2.666	2.666	0.000
Co−O	1.885	1.885	0.000
Orthorhombic Structure			
parameters	exp/Å	calcd/Å	Δ (exp − calcd)/Å
a	5.3312	5.3501	−0.0188
b	7.5482	7.5473	0.0008
c	5.3461	5.3347	0.0114
Nd−O(1)	2.30	2.37	−0.07
	2.49	2.53	−0.04
Nd−O(2)	2.35 (× 2)	2.38	−0.03
	2.56 (× 2)	2.65	−0.09
Co−O(1)	1.93	1.91	0.02
Co−O(2)	1.92 (× 2)	1.92	0.00
	1.94 (× 2)	1.92	0.02

3. Results and Discussion

3.1. Intrinsic Defects and Redox Properties. Schottky and Frenkel defect energies for both the cubic and orthorhombic structures were calculated using the appropriate energy terms according to the following equations (Kröger−Vink notation is used throughout):

Neodymium Frenkel disorder:

$$Nd_{Nd}^{\times} \rightarrow V_{Nd}''' + Nd_i^{\cdots} \quad (2)$$

Cobalt Frenkel disorder:

$$Co_{Co}^{\times} \rightarrow V_{Co}''' + Co_i^{\cdots} \quad (3)$$

Oxygen Frenkel disorder:

$$O_O^{\times} \rightarrow V_O^{\cdot\cdot} + O_i'' \quad (4)$$

$NdCoO_3$ Schottky disorder:

$$Nd_{Nd}^{\times} + Co_{Co}^{\times} + 3O_O^{\times} \rightarrow V_{Nd}''' + V_{Co}''' + 3V_O^{\cdot\cdot} + NdCoO_3 \quad (5)$$

The results are reported in Table 3.

TABLE 3: Energies of Frenkel and Schottky Disorder in $NdCoO_3$

		energy (eV/defect)	
reaction	equation	cubic	orthorhombic
Nd Frenkel	2	11.19	11.29
Co Frenkel	3	11.17	9.54
O Frenkel	4	3.50	4.53
$NdCoO_3$ Full Schottky	5	2.94	3.74

Full Schottky disorder is predicted to be the most favorable type of defect both in the cubic and orthorhombic structures (Table 3). However, the defect energies are all relatively high, suggesting that the concentration of intrinsic point defects in this compound is not substantial at room temperature. The two sets of results do not differ significantly, suggesting that the defect chemistries of the cubic and the orthorhombic structures are governed by the same mechanisms. In the discussion that follows, we thus focus only on the cubic structure.

A series of redox reactions in the undoped $NdCoO_3$ system were considered, and the energies of these processes were compared to determine the most likely reduction and oxidation mechanisms. Using an approach that has been successfully applied to other transition-metal oxides,[29,34] we treated the electronic defects, electrons (e') and holes ($h^{\cdot}$), as localized species (small polarons). For the undoped system, the following reactions for oxidation were considered.

$$3/2O_2 + 2Nd_{Nd}^{\times} \rightarrow 2V_{Nd}''' + 6h^{\cdot} + Nd_2O_3 \quad (6)$$

$$3/2O_2 + 2Co_{Co}^{\times} \rightarrow 2V_{Co}''' + 6h^{\cdot} + Co_2O_3 \quad (7)$$

$$3/2O_2 + Nd_{Nd}^{\times} + Co_{Co}^{\times} \rightarrow V_{Nd}''' + V_{Co}''' + 6h^{\cdot} + NdCoO_3 \quad (8)$$

With regard to the hole ($h^{\cdot}$) species, our calculations found that formation of a Co^{4+} species is more favorable than O^- formation (4.93 eV vs 8.18 eV), indicating that holes are centered on Co ions.

In addition to oxidation reactions, we also considered reduction in the undoped material, which can occur via loss of oxygen according to:

$$O_O^{\times} \rightarrow V_O^{\cdot\cdot} + \frac{1}{2}O_2 + 2e' \quad (9)$$

where the two electrons produced will partially reduce Co^{3+} to Co^{2+}.

The charge state of Co in rare-earth cobaltites has been the subject of considerable interest for many decades now. Experimental measurements of the electrical and optical properties of $LaCoO_3$ indicate that it is a small polaron conductor at room temperature. The complex temperature dependence of the Seebeck coefficient in $LaCoO_3$ can be successfully modeled assuming the formation of small polarons by charge disproportionation of the Co ion.[23] Moreover, progressive doping of the compound is known to decrease the disproportionation energy. For pure $LaCoO_3$, Rajoria et al.[23] estimated that about 40% of Co^{3+} has undergone disproportionation at a temperature of about 1000 K; doping also lowers the temperature at which disproportionation commences. The similarity between $LaCoO_3$ and $NdCoO_3$ means that such processes most likely occur in the latter as well. We therefore calculated the energy of disproportionation of Co^{3+}, in which two Co^{3+} ions change charge states to create a Co^{2+} (i.e., Co'_{Co}) and a Co^{4+} (i.e., $Co^{\cdot}_{Co}$) species, according to:

$$2Co_{Co}^{\times} \leftrightarrow Co'_{Co} + Co^{\cdot}_{Co} \quad (10)$$

TABLE 4: Calculated Energies of Redox Processes in Undoped $NdCoO_3$

process	equation	energy (eV/defect)
oxidation	6	7.84
oxidation	7	9.05
oxidation	8	7.74
reduction	9	3.15
disproportionation	10	1.80

The energies of these oxidation (eqs 6−8), reduction (eq 9), and disproportionation (eq 10) processes are reported in Table 4. Our calculations included all the key terms in the redox processes, but there are uncertainties in the absolute values obtained because of the free-ion energies employed. Nevertheless, our concern here is to understand how electronic species might form; for this task, our modeling methods have proven to be reliable.

Table 4 shows that reduction should occur more readily than oxidation, which is in good agreement with experimental results[21] and accounts for the under-stoichiometry of this compound under standard conditions. We predict that in the undoped compound, oxidation processes are unlikely to occur because the energies of the various oxidation reactions considered are all very high.

Interestingly, disproportionation is found to be the most favorable process in undoped $NdCoO_3$. This is consistent with Mössbauer measurements by Rajoria et al.[23] on $NdCoO_3$ doped with small amounts of Fe, which found mixed charge states for the transition-metal ions. A fraction of the Co in $NdCoO_3$ can therefore be expected to be present as Co^{2+} and Co^{4+}, in addition to Co^{3+}.

The ease of reduction and disproportionation in $NdCoO_3$ means that it will contain a mixture of Co^{2+} (as Co'_{Co}), Co^{4+} (as $Co^{\cdot}_{Co}$), and oxygen vacancies, particularly at high temperature. All these species have net charges relative to the ideal lattice, and all have been shown to contribute to conductivity in $LaCoO_3$.[23] The presence of a mixture of positive and negative electronic species (electrons and holes) can explain the unusual temperature dependence of electrical conductivity in $NdCoO_3$. Furthermore, our disproportionation energy is sufficiently high to be consistent with experimental observations that Co^{2+} and Co^{4+} species are not formed in large numbers until high temperatures are reached.[22,23]

The charged species resulting from reduction and disproportionation, being opposite in sign, are likely to interact with each other, so that formation of defect clusters might be expected. Some defect models have been proposed for the ordering of $[Co'_{Co} - V_O^{\cdot\cdot} - Co'_{Co}]^{\times}$ clusters in $LaCoO_3$, based on composition vs oxygen partial pressure data.[19] No evidence has been reported for the existence of $[Co'_{Co} - Co^{\cdot}_{Co}]^{\times}$ clusters, however. Using our simulation techniques, we analyzed various linear and square planar arrangements of Co'_{Co} and $V_O^{\cdot\cdot}$ species in $NdCoO_3$. Figure 1 shows examples of the types of clusters considered.

The binding (or association) energy of each cluster can be calculated with respect to the isolated component defects. Of those considered, neutral $[Co'_{Co} - V_O^{\cdot\cdot} - Co'_{Co}]^{\times}$ clusters resulted in negative binding energies (ca. −1.1 eV/defect), which suggests a significant degree of stability. This accords with experimental evidence[19] for the ordering of Co^{2+} and oxygen vacancies in similar systems. Charged clusters (such as $[Co'_{Co} - V_O^{\cdot\cdot}]^{\cdot}$) were slightly less stable. Table 5 also reveals that as the cluster size increases, square configurations become more stable than linear ones, as found for $[4Co'_{Co} - 2V_O^{\cdot\cdot}]^{\times}$.

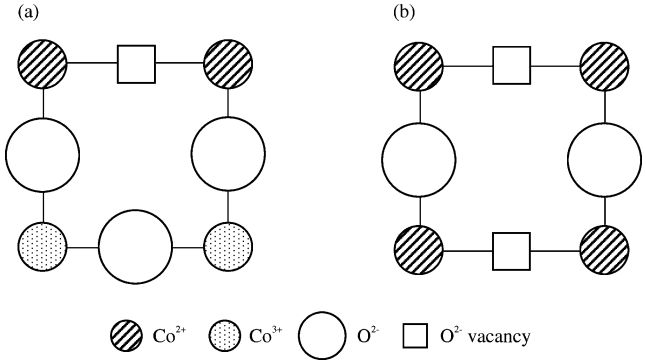

Figure 1. Examples of neutral $Co'_{Co} - V_O^{\cdot\cdot}$ clusters in $NdCoO_3$ (where Co'_{Co} is Co^{2+}); (a) linear configuration, (b) square configuration.

TABLE 5: Calculated Binding Energies for $Co'_{Co} - V_O^{\cdot\cdot}$ Clusters in Linear and Square Configurations

	binding energy (eV/defect)	
cluster	linear	square
$[Co'_{Co} - V_O^{\cdot\cdot}]^{\cdot}$	−0.83	
$[2Co'_{Co} - V_O^{\cdot\cdot}]^{\times}$	−1.09	
$[3Co'_{Co} - 2V_O^{\cdot\cdot}]^{\cdot}$	−0.21	
$[4Co'_{Co} - 2V_O^{\cdot\cdot}]^{\times}$	−0.08	−1.09

TABLE 6: Calculated Binding Energies for Neutral $Co'_{Co} - Co^{\cdot}_{Co}$ Clusters in Linear and Square Configurations

	binding energy (eV/defect)	
cluster	linear	square
$[Co'_{Co} - Co^{\cdot}_{Co}]^{\times}$	−0.26	
$[2Co'_{Co} - 2Co^{\cdot}_{Co}]^{\times}$	−0.38	−0.35
$[3Co'_{Co} - 3Co^{\cdot}_{Co}]^{\times}$	−0.61	−0.40
$[4Co'_{Co} - 4Co^{\cdot}_{Co}]^{\times}$		−0.42

We also calculated the energies of ordered neutral clusters of Co^{2+} and Co^{4+} arranged linearly along one of the crystallographic axes as well as planar arrangements consisting of two alternate rows. Figure 2 shows the types of clusters considered.

Results for the two types of arrangements are listed in Table 6. Strong binding energies are found for these types of clusters, particularly the linear configurations. There is a slight increase in the magnitude of the binding energy as the size of the cluster increases. This suggests possible short-range ordering of Co^{2+} and Co^{4+} defects if a sufficient concentration of these species is present.

3.2. Dopant Incorporation. Dopant cations can substitute for either Nd^{3+} or Co^{3+} in $NdCoO_3$. In the case of aliovalent (donor or acceptor) dopants, this requires the creation of charge-compensating defects. Experimentally, it can be difficult to determine which site a particular dopant favors, particularly if its ionic radius lies somewhere between those of the A and B lattice ions. Our simulation methods help resolve these issues by generating quantitative estimates of the relative energies of different mechanisms of incorporation or "solution". Although the prediction of the maximum amount of dopant that can be incorporated (i.e., its solid solubility limit) is less straightforward, our results can provide a useful systematic guide to the site selectivity of different dopant species and to trends in dopant solubility. Such an approach has been applied successfully to a variety of oxides,[26] including other perovskites.[28,34,37,38] We have therefore examined a wide range of dopants in $NdCoO_3$ including monovalent (e.g., Li^+ and Na^+), divalent (e.g., Sr^{2+} and Cu^{2+}), trivalent (e.g., Fe^{3+} and Mn^{3+}), and tetravalent (e.g., Ti^{4+} and Zr^{4+}) ions. The results are discussed in the following sections.

3.2.1. M^+ and M^{2+} Substitution. Monovalent and divalent dopants can potentially substitute on either the Nd or the Co site with the creation of oxygen vacancies for charge compensation. We present only the equations for substitution on the Nd site because equivalent charge compensation mechanisms were considered for substitution on the Co site:

$$\frac{1}{2}M_2O + Nd_{Nd}^{\times} + O_O^{\times} \rightarrow M''_{Nd} + V_O^{\cdot\cdot} + \frac{1}{2}Nd_2O_3 \quad (11)$$

$$MO + Nd_{Nd}^{\times} + \frac{1}{2}O_O^{\times} \rightarrow M'_{Nd} + \frac{1}{2}V_O^{\cdot\cdot} + \frac{1}{2}Nd_2O_3 \quad (12)$$

The incorporation energies for alkali and alkaline earth metal substitution in $NdCoO_3$ are plotted in Figure 3 as a function of dopant ionic radius.[39] These show that monovalent substitutions are unfavorable on both sites; solution energies are particularly high for substitution on the Co site and increase rapidly as the dopant ionic radius increases. For alkaline earths, the solution energies strongly depend on the dopant size. On the Nd site, Ca^{2+} and Sr^{2+} are predicted to be the most favorable dopants, as has been found previously for $LaCoO_3$.[34,38] This may explain why Sr^{2+} is the most common dopant used to enhance the catalytic and transport activity of this kind of material. However, whereas for $LaCoO_3$ the lowest solution energy is found for Sr^{2+} on the La site, we find that for $NdCoO_3$ the minimum energy is for Ca^{2+}, as might be expected from the relative differences in ionic radii between the two perovskites. It is worth noting that we also calculate a relatively low solution energy for Mg^{2+} on the B site, which suggests that the alkaline earth will preferentially substitute for Co^{3+} rather than Nd^{3+}.

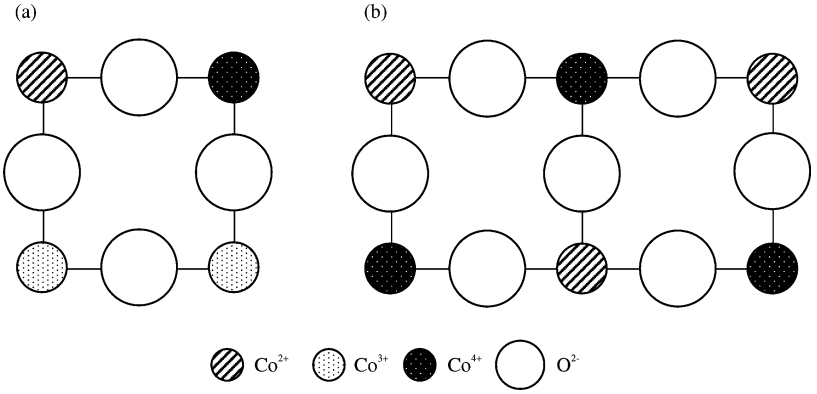

Figure 2. Examples of neutral $Co'_{Co} - Co^{\cdot}_{Co}$ clusters in $NdCoO_3$ (where Co'_{Co} is Co^{2+} and $Co^{\cdot}_{Co}$ is Co^{4+}); (a) linear configuration, (b) square configuration.

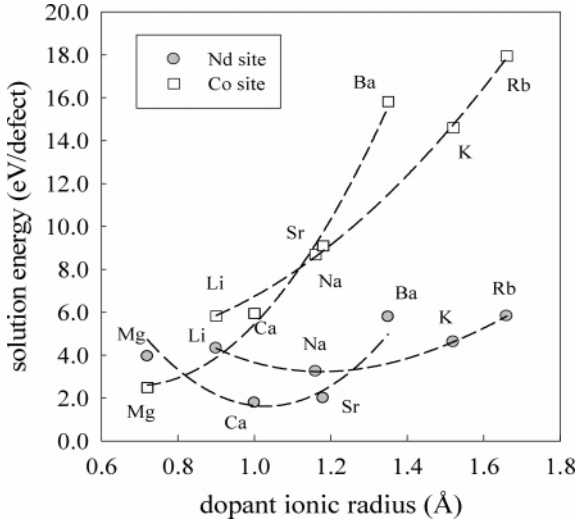

Figure 3. Solution energy vs dopant ionic radius for alkali and alkaline earth substitution in $NdCoO_3$. Lines are guides for the eyes only.

TABLE 7: Solution Energies of Divalent Transition-Metal Dopants in Cubic $NdCoO_3$

		solution energy (eV/dopant)	
dopant	ionic radius (Å)	Nd site	Co site
Ni^{2+}	0.690	4.94	3.32
Cu^{2+}	0.730	5.26	1.21
Zn^{2+}	0.740	3.97	2.95
Fe^{2+}	0.780	3.95	3.35
Mn^{2+}	0.830	3.13	3.65

In Table 7, the solution energies for divalent transition-metal ions are reported. Incorporation of these cations is in general more favorable on the Co site, with a particularly low energy for Cu^{2+}. This is consistent with experimental results showing that Cu is readily soluble in $LaCoO_3$, with the solid solution $La_{0.8}Sr_{0.2}Co_{1-x}Cu_xO_{3-\delta}$ extending over the entire range of x.[40] Moreover, for certain concentrations of Cu, enhancement of the catalytic activity of the material has been observed.

3.2.2. M^{3+} and M^{4+} Substitution. Isovalent (M^{3+}) dopants can substitute on either the Nd or the Co site without any charge compensation according to:

$$\frac{1}{2}M_2O_3 + Nd_{Nd}^{\times} \rightarrow M_{Nd}^{\times} + \frac{1}{2}Nd_2O_3 \qquad (13)$$

Figure 4 shows a plot of solution energy vs dopant ionic radius for M^{3+} substitution. As expected from ion-size arguments, smaller cations are favorable dopants on the Co site (with the lowest energy obtained for the smallest ion, Al^{3+}), whereas the larger cations substitute more favorably for Nd. Of those considered, the most favorable dopant on the Nd site is predicted to be Gd.

The introduction of an M^{4+} dopant on an Nd or Co site produces a defect with a net positive charge. Charge compensation could occur by either the formation of electronic species (as Co'_{Co}) or cation vacancies, according to the following equations:

$$MO_2 + Nd_{Nd}^{\times} \rightarrow M_{Nd}^{\cdot} + e' + \frac{1}{4}O_2 + \frac{1}{2}Nd_2O_3 \qquad (14)$$

$$MO_2 + \frac{4}{3}Nd_{Nd}^{\times} \rightarrow M_{Nd}^{\cdot} + \frac{1}{3}V_{Nd}''' + \frac{2}{3}Nd_2O_3 \qquad (15)$$

Our calculations predict that for this compound, the two mechanisms of charge compensation are essentially equivalent

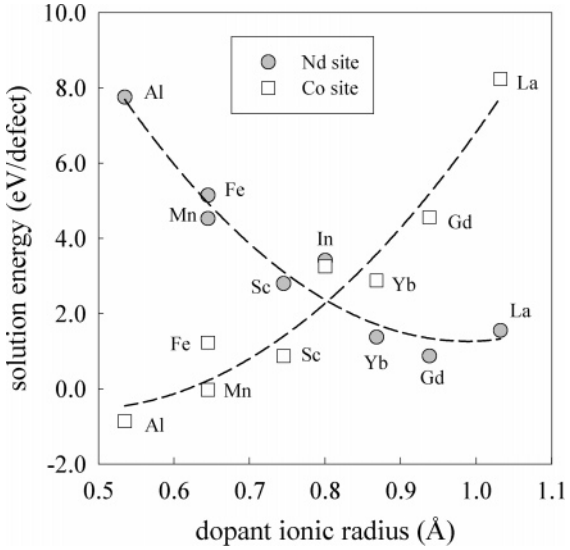

Figure 4. Solution energy vs dopant ionic radius for trivalent ion substitution in $NdCoO_3$. Lines are guides for the eyes only.

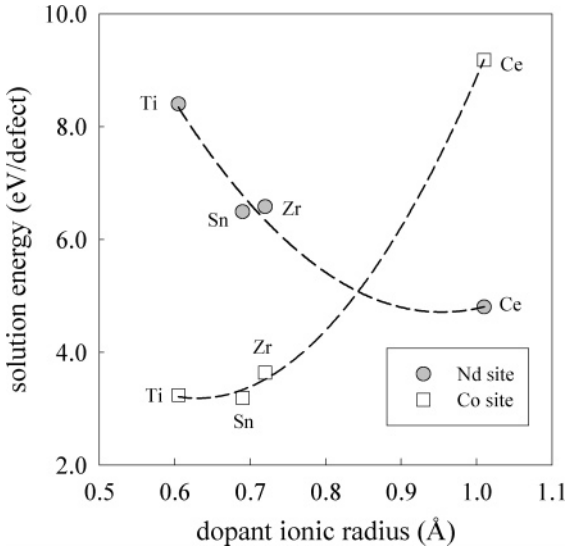

Figure 5. Solution energy vs dopant ionic radius for tetravalent ion substitution in $NdCoO_3$. Lines are guides for the eyes only.

(differences are about 0.4 eV, with a slight preference for the formation of electronic defects). However, all of the solution energies for M^{4+} substitution are high and unfavorable, particularly on the Nd site (Figure 5), suggesting that such doping would not be significant in the $NdCoO_3$ system. Not surprisingly, successful synthesis of Ce-doped $NdCoO_3$ has never been reported in the literature, whereas for the analogous $LaCoO_3$ system, up to 10% Ce can be substituted for La before a second phase forms.[41] Higher Ce contents always resulted in multiphase materials with phases such as CeO_2, Co_3O_4, and La_2CoO_4.[41]

3.3. Oxidation of Doped $NdCoO_3$. It is generally believed that the catalytic behavior (and the oxygen transport in the case of fuel cell electrodes) of a material is partly controlled by the exchange between gas-phase oxygen and the lattice oxygen of the doped perovskite system. In terms of defect chemistry, this takes place by the filling of oxygen vacancies by molecular oxygen from the atmosphere with the formation of electronic holes; such an oxidation reaction involves the dissociation of O_2 according to:

$$\frac{1}{2}O_2 + V_O^{\cdot\cdot} \rightarrow O_O^{\times} + 2h^{\cdot} \qquad (16)$$

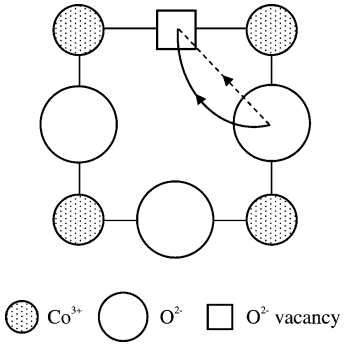

Figure 6. Schematic diagram comparing linear and curved trajectories for O^{2-} migration in $NdCoO_3$

In this case, large numbers of oxygen vacancies already exist in the lattice on account of aliovalent doping (e.g., with Sr^{2+} or Ca^{2+}).

The results favor (on energetic grounds) holes centered on Co ions (to form Co^{4+}) in $NdCoO_3$, because we derive a very small positive energy (0.46 eV/$h^{\cdot}$) for this oxidation reaction. Such a value is consistent with experimental results that show mixed (electronic and ionic) conductivity in the doped oxide and that the *p*-type electronic conductivity increases with increasing oxygen activity.

The high catalytic activity of doped $NdCoO_3$ may be attributed to the relative ease of oxidation and concomitant formation of Co^{4+}. Indeed, an important aspect of the behavior of various perovskites arises from the fact that a transition-metal ion on the B site can readily change its oxidation state. This typically allows the reversible addition and removal of oxygen, which enables the compound to act as an oxygen store in catalytic reactions.

3.4. Oxygen Vacancy Migration. The ionic conductivity of $NdCoO_3$ is mainly due to oxygen vacancy migration; thus, increasing the concentration of this species should result in an increased conductivity. As mentioned in the Introduction, high oxygen mobility in the bulk material is fundamental to the catalytic application of the material; atomistic simulation techniques are well-established tools for obtaining information about the mechanism and energetics of ion diffusion through the crystal lattice.

We have calculated energy profiles for vacancy migration between adjacent oxygen sites in $NdCoO_3$ by considering two scenarios; a linear path and a minimum-energy path. The latter is predicted to follow a curved trajectory whereby the oxygen moves away from the Co at the center of a given $Co-O_6$ octahedron (illustrated in Figure 6). Such behavior has been found in other perovskite-related structures such as the $LaGaO_3$-based oxide ion conductor LSGM.[28,38] Indeed, neutron scattering and diffraction studies[42,43] of pure and doped $LaGaO_3$ provide experimental confirmation of the curved path predicted by simulation methods. In addition to the $LaGaO_3$ system, we have predicted such a curved path for oxygen migration in earlier studies of other perovskite oxides (e.g., $LaCoO_3$, $LaScO_3$, and $LaYO_3$),[28,38] which will hopefully stimulate further investigations in this area. Although, in retrospect, a curved path makes complete sense from a structural point of view, we stress that our simulations help to provide a rationalization based on quantitative calculations on the atomic scale as opposed to qualitative assumptions.

In Figure 7, a comparison between the energy profiles obtained for the linear and curved paths is presented. Our results predict that the activation energy for oxygen migration in $NdCoO_3$ is about 0.5 eV for the curved path. This value is less

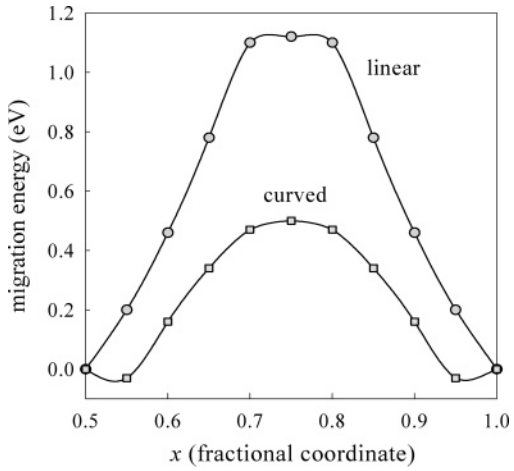

Figure 7. Energy profile for oxygen vacancy migration via linear and curved paths in $NdCoO_3$

TABLE 8: Calculated Binding Energies for Dopant-Defect Pair Clusters

Nd site		
	binding energies (eV/defect)	
dopant	$M'_{Nd} - V_O^{\cdot}$	$M'_{Nd} - h^{\cdot}$
Ca^{2+}	−0.16	−0.06
Sr^{2+}	−0.19	−0.09
Yb^{3+}	−0.31	−0.06
Gd^{3+}	0.11	−0.02
La^{3+}	0.22	0.03
Co site		
	binding energies (eV/defect)	
dopant	$M'_{Co} - V_O^{\cdot\cdot}$	$M'_{Co} - h^{\cdot}$
Mg^{2+}	−0.83	−0.58
Cu^{2+}	−0.59	−0.47
Zn^{2+}	−0.95	−0.53
Al^{3+}	−0.05	0.02
Fe^{3+}	−0.14	−0.06
Mn^{3+}	−0.08	−0.04
Sc^{3+}	−0.22	−0.10

than that previously reported for $LaCoO_3$ using the same simulation techniques[34] and, moreover, is in excellent agreement with the available experimental data of 48 ± 7 kJ/mol (0.50 eV) between 970 and 1200 °C for $Nd_{0.8}Sr_{0.2}CoO_3$.[44]

3.5. Dopant-Defect Association. Binding or association of the mobile species to dopants can be detrimental to the performance of the material. However, for most perovskite oxides, detailed atomic-scale information on defect clusters is limited because experimental determination of localized or short-ranged structures can be difficult. We have therefore carried out, for the first time, a series of calculations on defect pair clusters in doped $NdCoO_3$ to assess the likelihood of cluster formation in this system.

Binding energies for both dopant-oxygen vacancy and dopant-hole pair clusters (with defects on adjacent sites) were calculated as the difference between the cluster energy and the sum of the energies of the isolated defects. Only the most favorable dopants from each of the monovalent, divalent, and trivalent dopant classes (on the relevant sites) were considered. The results are listed in Table 8 and reveal three main features.

First, pair clusters with divalent cations on the Nd site (e.g., Ca or Sr) have much lower binding energies than those on the Co site (e.g., Mg or Cu). Hence, for the same dopant concentration, Sr and Ca should provide the highest oxide ion conductivity compared to other divalent species. Second, the binding energies

are in general lower for dopant-hole clusters on either site, regardless of the type of cation. This suggests less trapping of hole species compared to oxygen vacancies, which indicates that electronic transport should be relatively high regardless of the type of acceptor dopant used. Third, the results for divalent dopants on the Co site point to greater trapping of the oxygen vacancies, perhaps leading to lower oxide ion mobility (on account of a higher activation energy). This would also lead to two regions with different slopes in the conductivity Arrhenius plot; the slope of the high-temperature region depends only on the oxygen migration energy, whereas the slope in the low-temperature region is a function of the migration energy plus a binding energy term.

The calculated binding energies (Table 8) indicate a small degree of association for some of the trivalent (isovalent) dopants (e.g., Yb on Nd and Sc on Co), but not others (e.g., La on Nd and Mn on Co). These results suggest the importance of local "elastic strain" effects, in which the binding energy is dependent upon the ion-size mismatch between host and isovalent dopant. This is borne out here with the greater ion-size mismatch for Yb^{3+} (0.868 Å) on the larger Nd^{3+} site (0.983 Å) and Sc^{3+} (0.745 Å) on the small Co^{3+} site (0.61 Å).

4. Conclusions

Our atomistic simulation techniques have provided detailed insights into the defect and dopant properties of $NdCoO_3$. The results improve our understanding of the defect reactions, doping mechanisms, and oxide ion mobility in $NdCoO_3$, atomic-level phenomena relevant to the use of this material in electrochemical applications. Additionally, they provide information that is of significance to the magnetic and thermoelectric behavior of this and related cobalt-containing perovskites. The discussion has highlighted the following points:

(i) Disproportionation is predicted to be the most energetically favorable intrinsic defect process, although the relatively high energy of this reaction suggests that concentrations of Co^{2+} and Co^{4+} species will only become significant at high temperatures. Previous explanations of the complex electrical conductivity behavior of $NdCoO_3$ on the basis of disproportionation of the transition-metal ion are therefore supported by our simulation results.

(ii) Reduction of undoped $NdCoO_3$ via oxygen loss is also found to be a low-energy process, which explains the oxygen sub-stoichiometry of this compound observed experimentally. The electrons so-formed should also contribute to the total electrical conductivity.

(iii) Doping with acceptor ions creates oxygen vacancies, which are likely to be key sites with regard to catalytic activity, and should promote a high oxygen flux through the solid. Our calculations show that Ca and Sr have the lowest incorporation energies and substitute preferentially for Nd. For both of these dopants, their binding energies to oxygen vacancies and to hole species are low. This is consistent with the widespread use of Ca and Sr as additives in $NdCoO_3$ perovskite to enhance its catalytic and sensor performance. Divalent cations (e.g., Mg^{2+} and Cu^{2+}) on the Co site, in contrast, give rise to significant binding energies and can, thus, be expected to have a detrimental effect on the ionic transport properties of the material.

(iv) A small favorable endothermic energy was calculated for oxidation of acceptor-doped $NdCoO_3$ involving filling of oxygen vacancies by molecular oxygen and accompanied by formation of Co^{4+} hole species. This is consistent with experimental findings that *p*-type conductivity increases with increasing oxygen activity in this material. The high catalytic activity of doped $NdCoO_3$ can be partly attributed to the relatively favorable energetics of this process.

(v) The activation energy for oxygen vacancy migration in $NdCoO_3$ was calculated to be about 0.5 eV, in good agreement with the available conductivity data. This low value suggests $NdCoO_3$ can support the high oxygen mobility necessary for the application of this material in sensor and electrochemical devices.

Acknowledgment. This work was supported by the Italian Ministry of Scientific Research as part of an FISR 2002 project. We thank INSTM for financial and administrative support. L.M. is grateful to the Accademia Nazionale dei Lincei for financial support, and C.A.J.F. thanks the Leverhulme Trust for a postdoctoral fellowship.

References and Notes

(1) Steele, B. C. H. *Solid State Ionics* **1996**, *86*−*88*, 1223−1234.
(2) Lane, J. A.; Benson, S. J.; Waller, D.; Kilner, J. A. *Solid State Ionics* **1999**, *21*, 201−208.
(3) van Doorn, R. H. E.; Bouwmeester, H. J. M.; Burggraaf, A. J. *Solid State Ionics* **1998**, *111*(*3*−*4*), 263−272.
(4) Tejuca, L. G.; Fierro, J. L. G.; Tascon, J. M. D. *Adv. Catal.* **1989**, *36*, 237−328.
(5) Doshi, R.; Alcock, C. B.; Carberry, J. J. *Catal. Lett.* **1993**, *18*, 337−343.
(6) Forni, L.; Rossetti, I. *Appl. Catal., B* **2002**, *38*, 29−37.
(7) Jung, H. J.; Lim, J. T.; Lee, S. H.; Kim, Y. R.; Choi, J. G. *J. Phys. Chem. B* **1996**, *100*, 10243−10248.
(8) Baiker, A.; Marti, P. E.; Keusch, P.; Fritsch, E.; Reller, A. *J. Catal.* **1994**, *146*, 268−276.
(9) Lago, R.; Bini, G.; Pena, M. A.; Fierro, J. L. G. *J. Catal.* **1997**, *167*, 198−209
(10) Shimizu, Y.; Yamashita, N. *Sens. Actuators, B* **2000**, *64*, 102−106.
(11) Choudhary, V. R.; Mondal, K. C.; Mamman, A. S.; Joshi, U. A. *Catal. Lett.* **2005**, *100*, 271−276.
(12) Maignan, A.; Flahaut, D.; Hèbert, S. *Eur. Phys. J. B* **2004**, *39*, 145−148.
(13) Androulakis, J.; Migiakis, P.; Giapintzakis, J. *Appl. Phys. Lett.* **2004**, *84*, 1099−1101.
(14) Robert, R.; Romer, S.; Reller, A.; Weidenkaff, A. *Adv. Eng. Mater.* **2005**, *7*, 303−308.
(15) Hammer, D.; Wu, J.; Leighton, C. *Phys. Rev. B: Condens. Matter Mater. Phys.* **2004**, *69*, 134407.
(16) Stauffer, D. D.; Leighton, C. *Phys. Rev. B: Condens. Matter Mater. Phys.* **2004**, *70*, 214414.
(17) Liu, J.-M.; Ong, C. K. *Appl. Phys. Lett.* **1998**, *73*, 1047−1049.
(18) Vanitha, P. V.; Arulraj, A.; Santhosh, P. N.; Rao, C. N. R. *Chem. Mater.* **2001**, *12*, 1666−1670.
(19) van Roosmalen, J. A. M.; Cordfunke, E. H. P. *J. Solid State Chem.* **1991**, *93*, 212−219.
(20) De Souza, R. A.; Kilner, J. A. *Solid State Ionics* **1998**, *106*, 175−187.
(21) Chan, K. S.; Ma, J.; Jaenicke, S.; Chuah, G. K.; Lee, J. Y. *Appl. Catal. A* **1994**, *107*, 201−227.
(22) Sehlin, S. R.; Anderson, H. U.; Sparlin, D. M. *Phys. Rev. B: Condens. Matter Mater. Phys.* **1995**, *52*, 11681−11689.
(23) Rajoria, D. S.; Bhide, V. G.; Rao, G. R.; Rao, C. N. R. *J. Chem. Soc., Faraday Trans. 2* **1974**, *70*, 512.
(24) Rohnke, M.; Janek, J.; Kilner, J. A.; Chater, R. J. *Solid State Ionics* **2004**, *166*, 89−102.
(25) Malavasi, L.; Tealdi, C.; Flor, G.; Chiodelli, G.; Cervetto, V.; Montenereo, A.; Borella, M. *Sens. Actuators B* **2005**, *105*, 299−303.
(26) Tealdi, C.; Islam, M. S.; Malavasi, L.; Flor, G. *J. Solid State Chem.* **2004**, *177*, 4359−4367.
(27) Buscaglia, M. T.; Buscaglia, V.; Viviani, M.; Nanni, R. *J. Am. Ceram. Soc.* **2001**, *84*, 376−384.
(28) Islam, M. S. *Solid State Ionics* **2002**, *144*−*145*, 75−85.
(29) Fisher, C. A. J.; Islam, M. S. *J. Mater. Chem.* **2005**, *15*, 3200−3207.
(30) Gale, J. D. *J. Chem. Soc., Faraday Trans.* **1997**, *93*, 629−637.
(31) Catlow, C. R. A. In *Solid State Chemistry − Techniques*; Cheetham, A. K., Day, P., Eds.; Clarendon Press: Oxford, 1987.

(32) Dick, B. G.; Overhauser, A. W. *Phys. Rev.* **1958**, *112*, 90−103.
(33) Wold, A.; Ward, R. *J. Am. Chem. Soc.* **1954**, *76*, 1029−1030.
(34) Read, M. S. D.; Islam, M. S.; Watson, G. W.; King, F.; Hancock, F. E. *J. Mater. Chem.* **2000**, *10*, 2298−2305.
(35) Lewis, G. V.; Catlow, C. R. A. *J. Phys. C: Solid State Phys.* **1985**, *18*, 1149−1161.
(36) Taguchi, H. *J. Solid State Chem.* **1996**, *122*, 297−302.
(37) Islam, M. S.; Cherry, M.; Winch, L. J. *J. Chem. Soc., Faraday Trans.* **1996**, *92*, 479−482.
(38) Islam, M. S.; Slater, P. R.; Tolchard, J. R.; Dinges, T. *Dalton Trans.* **2004**, 3061−3066.
(39) Shannon, R. D. *Acta Crystallogr., Sect. A: Found. Crystallogr.* **1976**, *32*, 751.
(40) Chai, Y. L.; Ray, D. T.; Liu, H. S.; Dai, C. F.; Chang, Y. H. *Mater. Sci. Eng. A* **2000**, *293*, 39−45.
(41) Kirchnerova, J.; Alifanti, M.; Delmon, B. *Appl. Catal. A* **2002**, *231*, 65−80.
(42) Lerch, M.; Boysen, H.; Hansen, T. *J. Phys. Chem. Solids* **2001**, *62*, 444−455.
(43) Yashima, M.; Nomura, K.; Kageyama, H.; Yoshinori, M.; Chitose, N.; Adachi, K. *Chem. Phys. Lett.* **2003**, *380*, 391−396.
(44) Kharton, V. V.; Naumovich, E. N.; Vecher, A. A.; Nikolaev, A. V. *J. Solid State Chem.* **1995**, *120*, 128−136.